PHYSICS

Spin-dependent charge transport through 2D chiral hybrid lead-iodide perovskites

Haipeng Lu[1]*, Jingying Wang[2]*, Chuanxiao Xiao[1]*, Xin Pan[2], Xihan Chen[1], Roman Brunecky[3], Joseph J. Berry[1], Kai Zhu[1], Matthew C. Beard[1†], Zeev Valy Vardeny[2†]

Chiral-induced spin selectivity (CISS) occurs when the chirality of the transporting medium selects one of the two spin ½ states to transport through the media while blocking the other. Monolayers of chiral organic molecules demonstrate CISS but are limited in their efficiency and utility by the requirement of a monolayer to preserve the spin selectivity. We demonstrate CISS in a system that integrates an inorganic framework with a chiral organic sublattice inducing chirality to the hybrid system. Using magnetic conductive-probe atomic force microscopy, we find that oriented chiral 2D-layered Pb-iodide organic/inorganic hybrid perovskite systems exhibit CISS. Electron transport through the perovskite films depends on the magnetization of the probe tip and the handedness of the chiral molecule. The films achieve a highest spin-polarization transport of up to 86%. Magnetoresistance studies in modified spin-valve devices having only one ferromagnet electrode confirm the occurrence of spin-dependent charge transport through the organic/inorganic layers.

INTRODUCTION

Spintronics, which takes advantage of not only the carrier (electron or hole) charge but also the spin degrees of freedom, provides a promising direction for the next generation of information technologies and is of special interest to quantum computing constructs (*1*, *2*). The key challenge in a spintronic device is to control the spin-polarized electron density, that is, to manipulate the number of electrons with well-defined spin states. Methods to achieve the desired spin control include light-matter interactions, such as spin-polarized light absorption and emission (*3*, *4*), electrical spin injection and detection in spin valves (*5*), or the combination of light and electricity (e.g., spin-polarized light-emitting diode devices) (*6*–*9*); all of these processes have been demonstrated in traditional epitaxial-grown GaAs semiconductors.

Recently, hybrid organic-inorganic perovskite (HOIP) semiconductors are being considered as candidates for spintronic applications due to a large spin-orbit coupling (SOC) and controllable Rashba splitting (*4*, *10*–*12*). For example, Odenthal *et al.* (*13*) observe a spin-coherence lifetime in methyl ammonium Pb-iodide ($MAPbI_3$) thin films exceeding 1 ns at low temperature. Similarly, spin-optoelectronic devices based on HOIP have been proposed theoretically (*14*) and recently demonstrated experimentally (*15*). In that work, spin-polarized carriers are injected into methyl-ammonium lead bromide ($MAPbBr_3$) films from ferromagnetic (FM) electrodes in two types of spintronic-based devices, namely, a spin light–emitting diode and a spin valve (*15*). In addition to their beneficial optoelectronic properties, the solution processability and rich chemical tunability of HOIP systems make them particularly interesting for spintronic applications. For instance, their chemical structure, composition, and dimensionality can be systematically tuned through both the inorganic and organic constituents (*16*).

The unique tunability of HOIPs offers an unprecedented opportunity to directly incorporate chiral organic molecules in the production of a two-dimensional (2D)–layered hybrid perovskite thin film and/or crystal that induces chirality into the inorganic sublattice band edge states. Thus, there is an interesting opportunity to explore how chiral molecules embedded into the multilayers provide spin control within these hybrid semiconductors. Recently, 3% spin-polarized photoluminescence was demonstrated at zero magnetic field at 2 K in 2D Pb-Br perovskite multilayers that incorporated chiral organic molecules (*17*), indicating that the HOIP spintronic properties can be controlled by the chirality of the incorporated organic cations. However, it should be noted that the demonstrated spin-polarized photoluminescence is likely intrinsically limited in that system, as the $n = 1$ 2D chiral perovskite lacks photoluminescence emission, and a mixed system with $n = 2$ layers was needed to observe photoluminescence and polarized photoluminescence. Hence, a more direct manipulation and associated demonstration in a spintronic device based on chiral perovskites should be both intriguing and insightful.

Here, we focus on controlling spin transport within 2D-layerd chiral Pb-I perovskite systems. We demonstrate spin polarization of charge transport through the chiral perovskites by showing that the injected current is preferential to one of the spin states and depends on the handedness of the incorporated chiral organic molecules; thus, the hybrid chiral system acts as a spin filter. This phenomenon, known as chiral-induced spin selectivity (CISS) (*18*, *19*), has been demonstrated in self-assembled chiral monolayers such as helical DNA (*20*–*22*), oligopeptides (*23*, *24*), helicenes (*25*), and chiral quantum dots (*26*) and shows interesting spin-dependent (photo)electrochemistry (*27*–*29*). However, the requirement of an oriented monolayer to preserve the spin selectivity inherently limits the efficiency and practical utility. In this study, we demonstrate that by tuning the organic component in the HOIP system to produce a highly oriented 2D chiral perovskite thin film, vertical charge transport is strongly spin dependent. Since our system is composed of multilayer chiral organic ligands embedded in an inorganic sublattice, it is conceptually different from previous reports of the CISS effect. We subsequently fabricated spin valves having a single FM spin injector rather than two FM electrodes as in more traditional spin-valve devices. The successful demonstration

[1]Chemistry and Nanoscience Center, National Renewable Energy Laboratory, Golden, CO 80401, USA. [2]Department of Physics and Astronomy, University of Utah, Salt Lake City, UT 84112, USA. [3]Chemical and Bioscience Center, National Renewable Energy Laboratory, Golden, CO 80401, USA.
*These authors contributed equally to this work.
†Corresponding author. Email: matt.beard@nrel.gov (M.C.B.); val@physics.utah.edu (Z.V.V.)

of the high spin selectivity in such multilayer hybrid systems substantially expands the application of the CISS effect.

RESULTS

Synthesis and photophysics of chiral 2D perovskites

The introduction of a chiral aromatic amine induces chirality in 2D-layered lead halide perovskites (Fig. 1A) (*30*, *31*). We first synthesize single crystals of 2D chiral perovskite, (*R*/*S*/*rac*-)methylbenzylammonium lead iodide (*R*/*S*/*rac*-MBA)$_2$PbI$_4$, from a cooling method adapted from literature reports (*31*). Polycrystalline thin films of the chiral perovskite were subsequently prepared by spin casting a dimethylformamide (DMF) solution of the corresponding single crystals (see Materials and Methods). X-ray diffraction (XRD) data show that in these thin films, the 2D perovskite layers are highly oriented parallel to the substrate, with only (0 0 *2l*) peaks observed (Fig. 1B). Note that the crystallinity of both systems, (*R*- and *S*-MBA)$_2$PbI$_4$, appears to be comparable, with no additional impurity peaks being detected. The degree of crystallographic orientation is further confirmed by 2D XRD measurements (Fig. 1, C and D). Intense and sharp Bragg spots are observed in the (*R*- or *S*-MBA)$_2$PbI$_4$ films that indicates highly oriented crystal grains. The Bragg spots can be assigned to the diffraction from (0 0 *2l*) peaks, consistent with 1D XRD results. The (*rac*-MBA)$_2$PbI$_4$ and phenethylammonium lead iodide (PEA$_2$PbI$_4$) films also display similar 2D XRD patterns (fig. S1), suggesting a highly oriented crystal structure in all of the resulting thin films studied here.

Atomic force microscopy (AFM) is used to determine the morphology and thickness of the 2D-layered films. All the films have exceptionally low roughness with an R_q (root mean square average) of 1 to 3 nm, suggesting a very uniform morphology (Fig. 2, A and C). The film thickness based on a 10 weight % (wt %) solution is found to be ~50 nm (fig. S2). Linear absorption spectra show a characteristic exciton peak at ~500 nm (Fig. 2B), suggesting dielectric and quantum confinement in the 2D layers, similar to the previously studied more traditional 2D perovskite systems (*32*).

We also observe circular dichroism (CD) of the thin films. Transmission CD spectra display distinct derivative features for the (*R*-MBA)$_2$PbI$_4$ film (Fig. 2D, red trace) and the (*S*-MBA)$_2$PbI$_4$ film (Fig. 2D, blue trace), while (*rac*-MBA)$_2$PbI$_4$ film exhibits no CD (Fig. 2D, black trace). All the peaks in the CD spectra appear to be at the same wavelengths (at 215, 260, 310, 380, 497, and 508 nm) for (*R*- and *S*-MBA)$_2$PbI$_4$ films but with opposite signs. While the high-energy CD signals (at 215 and 260 nm) can be assigned to the optical activity of the isolated organic molecules (*R*-MBA and *S*-MBA), the low-energy CD response arises from the induced optical activity within the inorganic framework. This indicates that the incorporation of chiral organic amines leads to optical chirality in

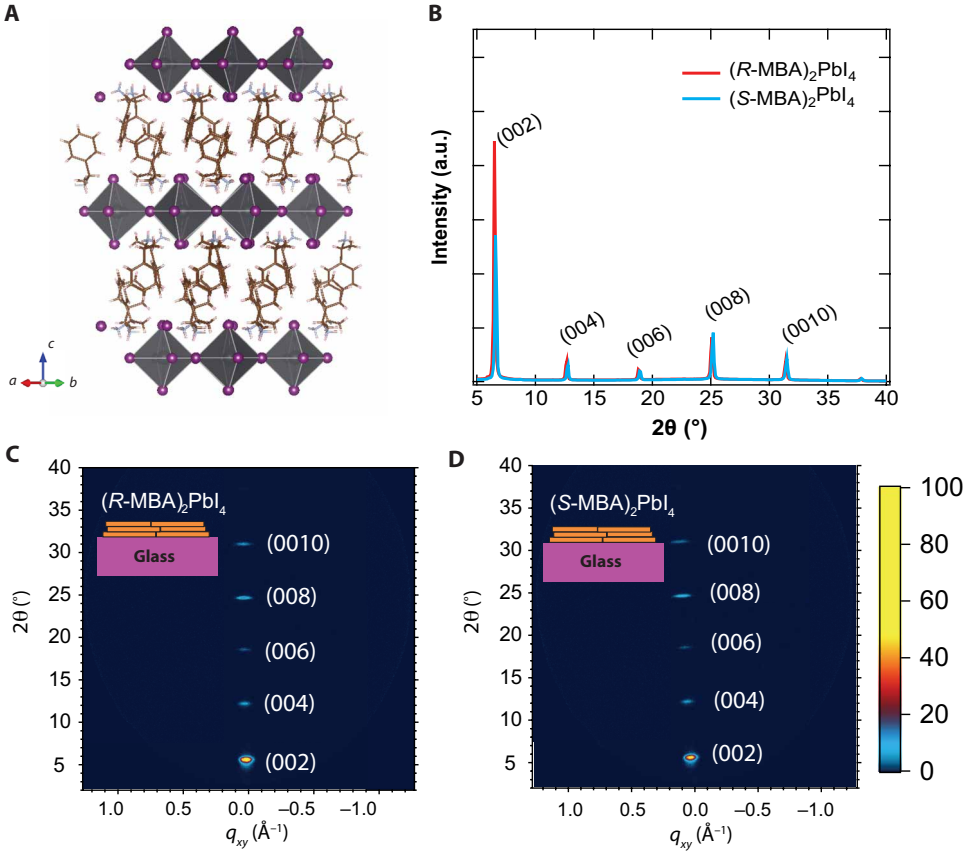

Fig. 1. Structure and crystallographic orientation characterization. (**A**) Crystalline structure (*30*) of chiral perovskite, (*R*/*S*-)methylbenzylammonium lead iodide (*R*/*S*-MBA)$_2$PbI$_4$. (**B** to **D**) Crystallographic orientation characterization of perovskite thin films: 1D (B) and 2D XRD patterns (C and D). Note that layers are highly oriented as only (0 0 *2l*) peaks are observed. Intense Bragg spots further indicate the layers oriented parallel to the substrates. Inset: Crystallographic orientation of perovskite layers. a.u., arbitrary units.

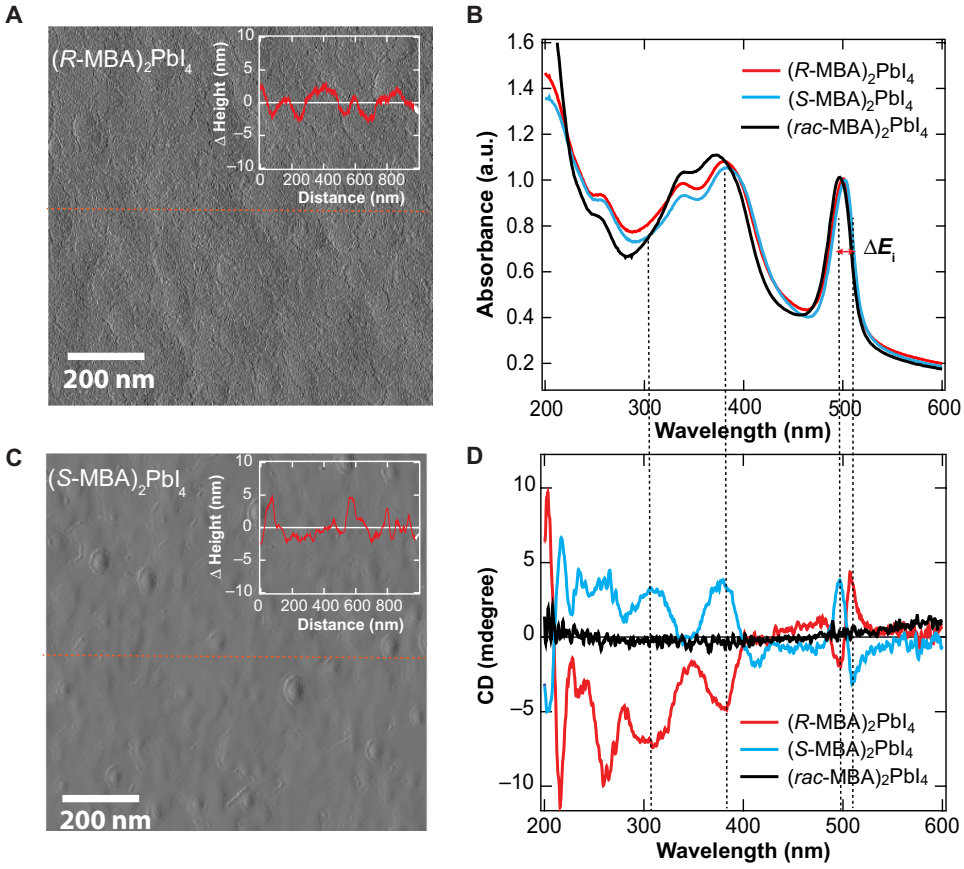

Fig. 2. Morphological and photophysical characterization. (**A** to **D**) AFM images of $(R\text{-MBA})_2PbI_4$ (A) and $(S\text{-MBA})_2PbI_4$ (C), respectively. Inset: AFM height profile of the red line drawn in the AFM image. (B) Linear absorption (quartz substrate) and (D) circular dichroism (CD) spectra (quartz substrate). CD spectra display derivative features at 200 to 600 nm, with $(R\text{-MBA})_2PbI_4$ and $(S\text{-MBA})_2PbI_4$ showing opposite signs.

the inorganic Pb-I framework. Our conclusion is supported by the derivative-like CD response around the band edge (at 497 and 508 nm), suggesting a lifting of the spin degeneracy within the band edge electronic states induced by the chiral molecules (i.e., the Cotton effect) (*33*). The exciton splitting energy (ΔE_i) is estimated to be 51 meV based on a Gaussian fitting of the CD and linear absorption spectra (fig. S3). Similar observations have been reported previously in chiral quantum dots (*33*), where the chirality is induced by surface chiral ligands (*34*, *35*). In the system examined by Ben-Moshe *et al.* (*33*), the exciton levels in the chiral quantum dots are split into two new sublevels ($\Delta E_i \sim 20$ to 50 meV) with opposite angular momentum, even in the absence of an external magnetic field. The origin of such exciton splitting in chiral quantum dots has been proposed to arise from a surface distortion–induced chirality (*35*) or the orbital hybridization of exciton levels of the quantum dots with the surface-bound molecular orbitals (*33*). The fundamental origin and precise mechanism of the optical activity within the 2D HOIP systems studied here remain unclear, requiring further investigation.

Magnetic conductive-probe AFM measurements

Spin-dependent charge transport properties in the chiral 2D perovskite films are assessed by conductive-probe AFM (CP-AFM) with an FM tip (Co-Cr coated). We prepared oriented chiral perovskite films by spin casting a DMF solution of perovskite crystals on fluorine-doped tin oxide (FTO) substrates (Fig. 3A). The FM tip can be magnetized by a permanent magnet with different magnetization directions (field-up or field-down with respect to the substrate), and the magnetized tip is subsequently used during the CP-AFM measurements. An electric bias potential is applied with respect to the FTO substrate, and the resulting current indicates electron transfer from the substrate to the tip through the 2D perovskite films. As the layers are orientated parallel to the substrate, vertical charge transport occurs when carriers tunnel from the inorganic layers through the organic chiral molecules. The helical potential in the chiral center controls the charge transfer rate for different spin polarities (*27*) of the tunneling carriers. Distinct from previously reported chiral self-assembled monolayer (SAM) systems (*26*), here, the carriers transfer through multiple vertical helical potentials in the thin 2D hybrid perovskite film (~50 nm) that consist of ~36 inorganic/organic layers. A similar concept was demonstrated by Naaman and co-workers (*36*) who found an increase in the spin selectivity with increasing length of the chiral molecule in the SAM. However, in our case, the spin selectivity through the multilayers is much stronger than through a monolayer or even a large DNA molecule.

The average current-voltage (*I*-*V*) curves measured for different 2D perovskite films under various magnetization directions are shown in Fig. 3 (B to D). All the measurements are conducted at room temperature. The solid traces represent the average of over 100 scans, while the shaded region around the traces is the statistical 95% confidence limits (fig. S4). All the *I*-*V* curves display an "S"

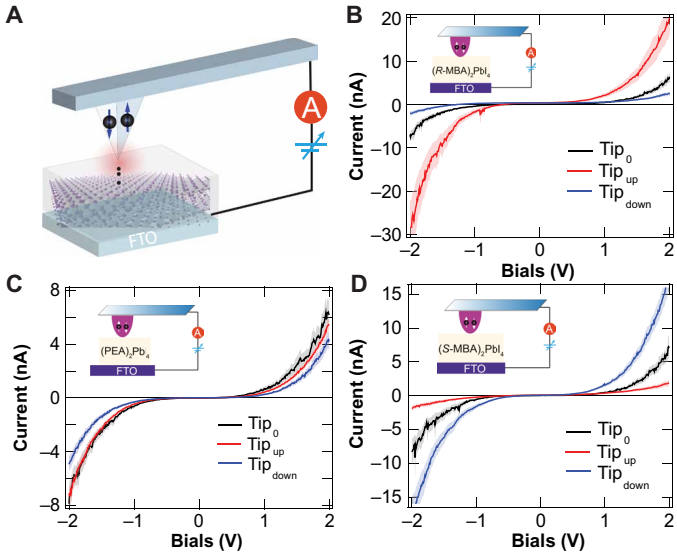

Fig. 3. mCP-AFM measurements. Schematic illustration of magnetic conductive-probe AFM (mCP-AFM) measurements (**A**) and chirality dependence in out-of-plane charge transport (**B** to **D**). Room-temperature *I-V* curves obtained using the mCP-AFM technique of chiral 2D hybrid perovskite thin films (~50 nm thick) for $(R\text{-MBA})_2PbI_4$ (B), $(S\text{-MBA})_2PbI_4$ (D), and nonchiral perovskite film PEA_2PbI_4 (C). The tip is magnetized in the north (blue), south (red), and nonmagnetized (black). The *I-V* response for each 2D film was averaged over 100 scans, and the shaded region around the lines marks the 95% confidence limits for the average results.

shape behavior, suggesting that charge transport occurs through a double-barrier tunneling potential (*26*). For the $(R\text{-MBA})_2PbI_4$ film, much higher current is measured when the tip is magnetized in the "up" direction versus that in the "down" direction (fig. S3B). That is, carriers with their spin oriented parallel to the tip magnetization direction are preferentially transferred from the FTO to the magnetized tip over those with antiparallel spin orientation. The opposite behavior is observed for the $(S\text{-MBA})_2PbI_4$ film, where higher current is observed when the tip is magnetized in the down direction as compared to the up direction (Fig. 3D). In contrast, nonchiral PEA_2PbI_4 films show little, if any, preference for the different tip magnetization direction (Fig. 3C).

To quantify the anisotropy of the polarized currents that we measure, we define a spin polarization, *P*, (*30*, *33*)

$$P = \frac{I_+ - I_-}{I_+ + I_-} \times 100\% \quad (1)$$

where I_+ and I_- are the measured currents at −2 V when the tip magnetic field is pointing up or down, respectively. Our CP-AMF result gives an exceptionally high spin polarization, *P*, of +86% and −84% for $(R\text{-MBA})_2PbI_4$ and $(S\text{-MBA})_2PbI_4$ films, respectively. Such spin polarization is significantly higher than that reported for chiral SAM systems (typically in the range of 30 to 50%) (*26*, *27*, *36*), thus supporting our hypothesis of improved spin selectivity through multiple chiral tunneling process. The multilayer configuration of the hybrid 2D layers allows the study of the thickness dependence of the spin polarization. We find that the spin polarization, *P*, exhibits a weak, if any, dependence on the film thickness. That is, *P* is consistently high (86 to 92%) for $(R\text{-MBA})_2PbI_4$ films, with varying thickness from 28 to 75 nm (fig. S5). The weak dependence on film thickness likely indicates that the spin selectivity saturates within a few tunneling events; thus, thicker films can no longer induce higher spin selectivity.

Studies of spin-valve devices based on chiral 2D hybrid perovskite interlayer

The CISS effect is also studied in spin-valve devices, using a single FM electrode instead of two FM electrodes as in more traditional spin valves. We fabricated spintronic devices with one FM electrode (NiFe) and a nonmagnetic electrode [indium tin oxide (ITO)] separated by a 2D hybrid perovskite film, as schematically illustrated in the inset of Fig. 4. The 2D perovskites are either chiral with opposite handedness or nonchiral (see Materials and Methods). The device resistance was measured at a temperature of 10 K upon application of an out-of-plane external magnetic field having strength, *B*. The resistance as a function of magnetic field, which is dominated by the magnetoresistance (MR) response of the three devices based on $(R\text{-MBA})_2PbI_4$, $(S\text{-MBA})_2PbI_4$, and $(PEA)_2PbI_4$ interlayers, is shown in Fig. 4 (A to C). The MR is defined by (*26*)

$$\text{MR} = \frac{R(B) - R(0)}{R(0)} \times 100\% \quad (2)$$

The difference in the MR(*B*) response of the various devices with different chirality is observed. First, the $(R\text{-MBA})_2PbI_4$– and $(S\text{-MBA})_2PbI_4$–based devices show opposite MR(*B*) responses. Second, the MR(*B*) response follows the hysteresis loop of the FM electrode, since the spin polarization of the injected carriers is proportional to the magnetization of the NiFe electrode. The opposite MR(*B*) response for devices based on layers with opposite chirality demonstrates that the injected spin-polarized carriers from the FM electrode move through the chiral perovskite layers while experiencing CISS. This is reflected in the electrical resistance that is different for carriers with opposite spins. In contrast, the MR(*B*) response of the device based on nonchiral $(PEA)_2PbI_4$ does not show the same response as those based on the chiral systems. As seen in Fig. 4C, it does not follow the NiFe magnetization response and thus has no CISS. Instead, the MR(*B*) response of this device results from an anisotropic MR of the FM electrode (*37*).

DISCUSSION

The spin selectivity observed here results from spin-polarized tunnel barriers formed by the chiral organic layers. The 2D-layered system forms multilayers of alternating inorganic and organic barrier layers (see Fig. 1A). The tunnel barrier height for carrier transport through the organic layers depends on the spin and the handedness of the chiral molecules (*18*). We hypothesize that the injected spin aligned carriers are mainly holes because the work functions of NiFe and ITO are both close to the valence band maximum of 2D perovskites (see fig. S6). These spin-polarized tunneling barriers act as a spin filter, preferentially promoting tunneling of one spin orientation. The MR response of the spintronic devices is therefore consistent with the magnetic CP-AFM (mCP-AFM) measurements (Fig. 3) and originates from CISS in the tunneling regime (*38*).

We performed a thickness-dependent MR study (see Fig. 5A). The MR response shows a weak dependence on the film thickness similar to that observed for the mCP-AFM measurements discussed above. The maximum MR value, MR_{max} versus thickness $MR_{max}(d)$ response, is substantially different from that observed in traditional spin-valve devices, in which $MR_{max}(d)$ decreases exponentially with

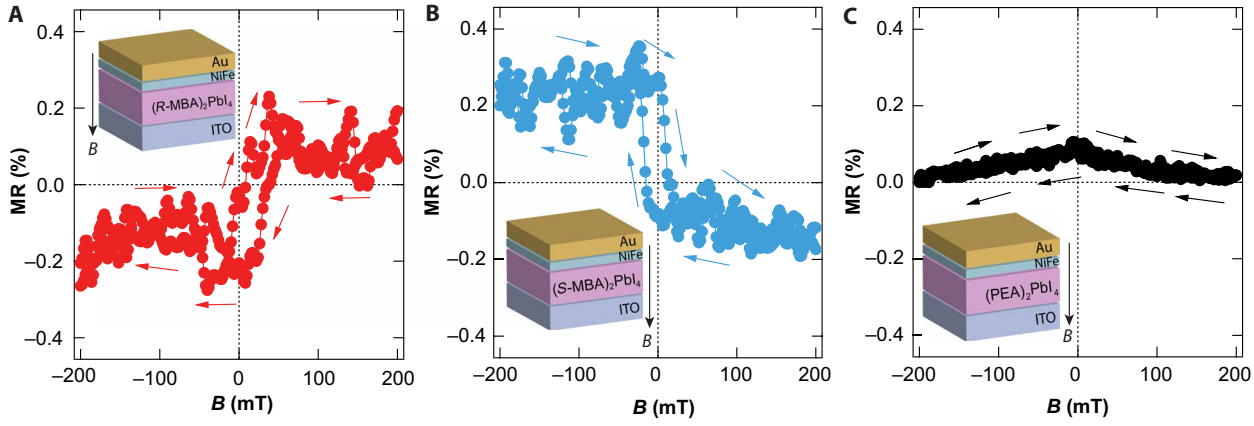

Fig. 4. MR response of spintronic devices based on chiral perovskites and schematic illustration of the device structure. MR(*B*) response of spintronic devices based on (*R*-MBA)$_2$PbI$_4$ (**A**), (*S*-MBA)$_2$PbI$_4$ (**B**), and (PEA)$_2$PbI$_4$ (**C**). The out-of-plane magnetic field was swept from −200 and 200 mT and back. The resistance was measured at an applied forward voltage of 0.5 V and a temperature of 10 K. The interlayer perovskite film thickness was ~60 nm for all devices.

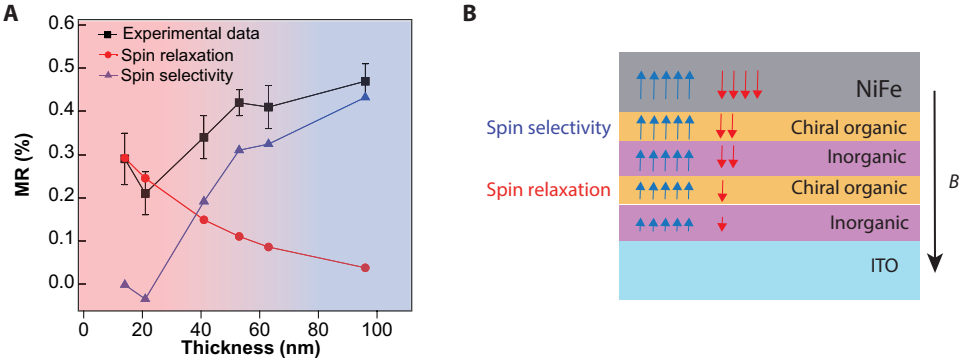

Fig. 5. Thickness-dependent MR study and schematic diagram of the spin transport through the 2D chiral perovskite layers. The MR$_{max}$(*d*) response is decomposed into two components in spintronic devices based on (*S*-MBA)$_2$PbI$_4$ with different thicknesses (**A**). The black squares are experimental MR$_{max}$(*d*), whereas the red circles are simulation of spin relaxation process (exponential decay with thickness, assuming a spin diffusion length of ~40 nm) (*39*). The difference between the black squares and red circles are represented by the blue triangles, which is a rough estimation of the spin selectivity dependence with the thickness. These two competing effects are illustrated in (**B**). Spin selectivity occurs through each chiral layer, whereas spin relaxation happens mainly through each inorganic layer that has strong SOC.

thickness due to the process of spin decoherence as carriers transverse by diffusion a nonchiral medium. In our case, the slight thickness dependence is likely due to competing effects that occur for thicker films. On the one hand, more tunnel barriers induce a higher spin selectivity. However, spin-lattice relaxation process occurs simultaneously during the spin-selective transport process. Therefore, the thickness dependence is a result of two competing processes, namely, spin-selective increase due to the increase in the number of chiral barrier layers and spin relaxation due to spin scattering (Fig. 5B). To further separate these two counteracting effects (CISS versus spin relaxation), we have developed a semiquantitative model assuming a simple exponential decay function that represents the process of the spin decoherence upon diffusion in the perovskite layer. The difference between the measured MR$_{max}$(*d*) and the simulated spin relaxation with *d* indicates the contribution from CISS (Fig. 5A). Although it is a rough estimation, it is seen that the spin selectivity is enhanced as the film thickness increases (Fig. 5A). In addition, the MR response does not show clear bias voltage dependence (see fig. S7). This is also in contrast with the MR response versus bias in traditional spin-valve devices, in which the MR response decreases significantly with increasing bias voltage (*39*). This demonstrates that the transport of spin-polarized carriers in the chiral hybrid layers is governed by a tunneling process and is therefore different from the spin-injection mechanism that occurs in a prototypical spin valve.

In conclusion, we show that the spin transport in 2D HOIPs can be effectively manipulated upon introducing chiral molecules into the organic spacer layers in the multilayer structures, which occur via the CISS mechanism. mCP-AFM studies demonstrate that charge transport through oriented chiral 2D perovskite is highly selective depending on the induced magnetization of the probe tip and the handedness of the embedded chiral organic molecules. The spin selectivity is observed to be much larger than previously reported in chiral SAM systems, as carriers transfer through multiple chiral layers of spin-polarized tunneling process. MR measurements in spintronic devices further confirm the spin-filtering effect enabled by the chiral organic layers, forming spin-valve devices based on a single FM electrode. The successful demonstration of CISS effect in the solution-processed polycrystalline 2D chiral perovskite films opens the door for future spintronic applications of chiral materials.

MATERIALS AND METHODS

Materials

All chemicals were used as received unless otherwise indicated. (*R*)-(+)-α-methylbenzylamine (*R*-MBA, 98%, ee 96%), (*S*)-(−)-α-methylbenzylamine (*S*-MBA, 98%, ee 98%), (±)-α-methylbenzylamine (*rac*-MBA, 99%), lead oxide (PbO, 99.999%), *N*,*N*-anhydrous DMF, and 57% aqueous hydriodic acid (HI) solution (99.95%, distilled, stabilized by H_3PO_2) were purchased from Sigma-Aldrich. Phenethylammonium iodide (PEAI) was purchased from GreatCell Solar.

Synthesis of (*R*-MBA)$_2$PbI$_4$, (*S*-MBA)$_2$PbI$_4$, and (*rac*-MBA)$_2$PbI$_4$ single crystals

The synthesis of the 2D chiral perovskite single crystals was adapted from literature reports (*31*). In general, 200 mg of PbO (0.897 mmol), 200 μl (1.57 mmol) of *R*-, *S*-, or *rac*-MBA, and 6 ml of HI solution were loaded into a glass vial. The as-formed yellow precipitates were subsequently dissolved at 90°C in an oil bath. The solution was slowly cooled to room temperature with a cooling rate of 1°C/hour, giving orange needles. These crystals were vacuum-filtrated and rinsed with diethyl ether. The final product was dried in vacuum overnight.

Synthesis of (PEA)$_2$PbI$_4$ single crystals

2D achiral perovskite $(PEA)_2PbI_4$ single crystals were synthesized on the basis of previously reported cooling method (*4*). Briefly, 127 mg (0.57 mmol) of PbO and 286 mg (1.15 mmol) of PEAI were fully dissolved in 10 ml of HI solution at 90°C. The solution was then slowly cooled to room temperature at a rate of 1°C/hour, giving orange sheet-like crystals. The crystals were then isolated from the parent solution by vacuum filtration and dried under vacuum.

Preparation of (*R*-MBA)$_2$PbI$_4$, (*S*-MBA)$_2$PbI$_4$, (*rac*-MBA)$_2$PbI$_4$, and PEA$_2$PbI$_4$ thin films

Glass, quartz, FTO (resistance, <25 ohm), or ITO substrates were washed sequentially by acetone and isopropanol in a sonicator for 10 min each, followed by an ultraviolet-ozone treatment for 15 min. The precursor solutions were prepared by dissolving the corresponding perovskite crystals in DMF with various concentrations (10 wt % for the mCP-AFM measurements). Thin films were then prepared by spin coating the precursor solution onto substrates using a spin rate of 4000 rpm for 30 s, followed by annealing at 100°C for 10 min. Thin films on glass substrates were used for XRD and AFM measurements. Thin films on quartz substrates were used for optical (linear absorption and CD) measurements. Thin films on FTO or ITO were used for mCP-AFM and MR measurements.

XRD measurements

Traditional θ/2θ XRD measurements of the thin-film systems were taken on a Rigaku DMax 2200 diffractometer with a rotating Cu anode. Complementary 2D XRD measurements to assess texture were taken with a Bruker D8 Discovery system with a GADDS (General Area Detector Diffraction System) four-circle detector and fixed Cu source.

CD measurements

CD measurements were carried out using a Jasco J-715 spectropolarimeter with the thin film placed in the beam path. The spectra obtained were averages of five scans. The spectra were smoothed using an internal algorithm in the Jasco software package, J-715 for Windows. The CD spectra of different constructs were monitored from 200 to 600 nm with 0.2-nm resolution, and the data were presented as the raw CD signal.

AFM measurements

The AFM topography images were taken by tapping mode with silicon cantilever (spring constant, ~42 N/m) at a resonant frequency of 200 to 400 kHz. The depth profile AFM sample was prepared by vertically scratching the sample surface with a new blade.

mCP-AFM measurements

Conductive-AFM results were collected by a Veeco D5000 AFM system in an Ar-filled glovebox equipped with the NanoScope V controller. A Bruker MESP-V2 tip (spring constant, ~3 N/m) was used in contact mode, and the Co-Cr–coated tips were premagnetized by a strong permanent magnetic for >30 min and then used for the scan immediately. The tip was placed back to the same pole of magnetic again for 30 min if measurement time was longer than 60 min. *I*-*V* curves were acquired by ramping the voltage from −2 to +2 V, with a frequency of 0.5 Hz. The bias voltage was applied to the sample, where the tip was virtually grounded. We used one magnetized tip to scan the three types of samples; and after scanning on all samples, we rescan the first sample to confirm that there is no significant change of the tip. With the tip magnetized by different field orientations (magnetic south, north, and no magnetic), we took more than 100 *I*-*V* curves from different locations on each sample.

Device fabrication and MR measurements

The ITO bottom electrode on glass substrate was patterned by wet etch photolithography. The ITO electrode was cleaned by sonication in acetone and isopropanol for 15 min. Subsequently, the bottom electrode was treated by oxygen plasma for 10 min. The chiral perovskite film was spin-coated on the pretreated ITO electrode inside a N_2-filled glovebox (O_2/H_2O < 1 parts per million). The chiral perovskite film was then annealed at 100°C for 10 min. After cooling down to ambient temperature, the sample was transferred to a vacuum chamber at a pressure of 10^{-7} torr for electron beam deposition of a 5-nm NiFe film as the top electrode in a cross-sectional configuration. Last, a 30-nm-thick Au film was coated for encapsulation purpose. The device area was 1 mm by 1 mm.

Following the fabrication process, the spin valve–like device was transferred to a closed-cycle cryostat for transport measurements. All the measurements were performed at 10 K. The device resistance was measured by a standard four-point method with Keithley 236 power supply and Keithley 2000 multimeter, while an out-of-plane magnetic field up to 200 mT was applied for MR measurements.

SUPPLEMENTARY MATERIALS

Supplementary material for this article is available at http://advances.sciencemag.org/cgi/content/full/5/12/eaay0571/DC1

Fig. S1. 2D XRD patterns for different 2D perovskite thin films.
Fig. S2. AFM images of different 2D perovskite thin films.
Fig. S3. Estimation of exciton splitting energy.
Fig. S4. Raw and averaged *I*-*V* curves from the mCP-AFM measurements.
Fig. S5. Thickness dependence of mCP-AFM studies.
Fig. S6. Schematic energy diagram of the "half spin valve" device based on the chiral 2D perovskite thin films.
Fig. S7. Voltage-dependent MR studies based on chiral (*R*-MBA)$_2$PbI$_4$ and (*S*-MBA)$_2$PbI$_4$ thin films.
Reference (*40*)

REFERENCES AND NOTES

1. S. A. Wolf, D. D. Awschalom, R. A. Buhrman, J. M. Daughton, S. von Molnár, M. L. Roukes, A. Y. Chtchelkanova, D. M. Treger, Spintronics: A spin-based electronics vision for the future. *Science* **294**, 1488–1495 (2001).
2. F. Pulizzi, Spintronics. *Nat. Mater.* **11**, 367 (2012).
3. R. Wang, S. Hu, X. Yang, X. Yan, H. Li, C. Sheng, Circularly polarized photoluminescence and Hanle effect measurements of spin relaxation in organic–inorganic hybrid perovskite films. *J. Mater. Chem. C* **6**, 2989–2995 (2018).
4. X. Chen, H. Lu, Z. Li, Y. Zhai, P. F. Ndione, J. J. Berry, K. Zhu, Y. Yang, M. C. Beard, Impact of layer thickness on the charge carrier and spin coherence lifetime in two-dimensional layered perovskite single crystals. *ACS Energy Lett.* **3**, 2273–2279 (2018).
5. M. Johnson, Spin accumulation in gold films. *Phys. Rev. Lett.* **70**, 2142–2145 (1993).
6. I. Malajovich, J. M. Kikkawa, D. D. Awschalom, J. J. Berry, N. Samarth, Coherent transfer of spin through a semiconductor heterointerface. *Phys. Rev. Lett.* **84**, 1015–1018 (2000).
7. I. Malajovich, J. J. Berry, N. Samarth, D. D. Awschalom, Persistent sourcing of coherent spins for multifunctional semiconductor spintronics. *Nature* **411**, 770–772 (2001).
8. H. J. Zhu, M. Ramsteiner, H. Kostial, M. Wassermeier, H. P. Schönherr, K. H. Ploog, Room-temperature spin injection from Fe into GaAs. *Phys. Rev. Lett.* **87**, 016601 (2001).
9. T. D. Nguyen, E. Ehrenfreund, Z. V. Vardeny, Spin-polarized light-emitting diode based on an organic bipolar spin valve. *Science* **337**, 204–209 (2012).
10. Y. Zhai, S. Baniya, C. Zhang, J. Li, P. Haney, C.-X. Sheng, E. Ehrenfreund, Z. V. Vardeny, Giant Rashba splitting in 2D organic-inorganic halide perovskites measured by transient spectroscopies. *Sci. Adv.* **3**, e1700704 (2017).
11. M. Kepenekian, J. Even, Rashba and Dresselhaus couplings in halide perovskites: Accomplishments and opportunities for spintronics and spin–orbitronics. *J. Phys. Chem. Lett.* **8**, 3362–3370 (2017).
12. D. Niesner, M. Wilhelm, I. Levchuk, A. Osvet, S. Shrestha, M. Batentschuk, C. Brabec, T. Fauster, Giant Rashba splitting in $CH_3NH_3PbBr_3$ organic-inorganic Perovskite. *Phys. Rev. Lett.* **117**, 126401 (2016).
13. P. Odenthal, W. Talmadge, N. Gundlach, R. Wang, C. Zhang, D. Sun, Z.-G. Yu, Z. Valy Vardeny, Y. S. Li, Spin-polarized exciton quantum beating in hybrid organic–inorganic perovskites. *Nat. Phys.* **13**, 894–899 (2017).
14. M. Kepenekian, R. Robles, C. Katan, D. Sapori, L. Pedesseau, J. Even, Rashba and Dresselhaus effects in hybrid organic–inorganic perovskites: From basics to devices. *ACS Nano* **9**, 11557–11567 (2015).
15. J. Wang, C. Zhang, H. Liu, R. McLaughlin, Y. Zhai, S. R. Vardeny, X. Liu, S. McGill, D. Semenov, H. Guo, R. Tsuchikawa, V. V. Deshpande, D. Sun, Z. V. Vardeny, Spin-optoelectronic devices based on hybrid organic-inorganic trihalide perovskites. *Nat. Commun.* **10**, 129 (2019).
16. B. Saparov, D. B. Mitzi, Organic–inorganic perovskites: Structural versatility for functional materials design. *Chem. Rev.* **116**, 4558–4596 (2016).
17. G. Long, C. Jiang, R. Sabatini, Z. Yang, M. Wei, L. N. Quan, Q. Liang, A. Rasmita, M. Askerka, G. Walters, X. Gong, J. Xing, X. Wen, R. Quintero-Bermudez, H. Yuan, G. Xing, X. R. Wang, D. Song, O. Voznyy, M. Zhang, S. Hoogland, W. Gao, Q. Xiong, E. H. Sargent, Spin control in reduced-dimensional chiral perovskites. *Nat. Photonics.* **12**, 528–533 (2018).
18. R. Naaman, D. H. Waldeck, Chiral-induced spin selectivity effect. *J. Phys. Chem. Lett.* **3**, 2178–2187 (2012).
19. R. Naaman, D. H. Waldeck, Spintronics and chirality: Spin selectivity in electron transport through chiral molecules. *Ann. Rev. Phys. Chem.* **66**, 263–281 (2015).
20. K. Senthil Kumar, N. Kantor-Uriel, S. P. Mathew, R. Guliamov, R. Naaman, A device for measuring spin selectivity in electron transfer. *Phys. Chem. Chem. Phys.* **15**, 18357–18362 (2013).
21. S. G. Ray, S. S. Daube, G. Leitus, Z. Vager, R. Naaman, Chirality-induced spin-selective properties of self-assembled monolayers of DNA on gold. *Phys. Rev. Lett.* **96**, 036101 (2006).
22. B. Göhler, V. Hamelbeck, T. Z. Markus, M. Kettner, G. F. Hanne, Z. Vager, R. Naaman, H. Zacharias, Spin selectivity in electron transmission through self-assembled monolayers of double-stranded DNA. *Science* **331**, 894–897 (2011).
23. J. J. Wei, C. Schafmeister, G. Bird, A. Paul, R. Naaman, D. H. Waldeck, Molecular chirality and charge transfer through self-assembled scaffold monolayers. *J. Phys. Chem. B* **110**, 1301–1308 (2006).
24. I. Carmeli, V. Skakalova, R. Naaman, Z. Vager, Magnetization of chiral monolayers of polypeptide: A possible source of magnetism in some biological membranes. *Angew. Chem. Int. Ed.* **41**, 761–764 (2002).
25. V. Kiran, S. P. Mathew, S. R. Cohen, I. Hernández Delgado, J. Lacour, R. Naaman, Helicenes—A new class of organic spin filter. *Adv. Mater.* **28**, 1957–1962 (2016).
26. B. P. Bloom, V. Kiran, V. Varade, R. Naaman, D. H. Waldeck, Spin selective charge transport through cysteine capped CdSe quantum dots. *Nano Lett.* **16**, 4583–4589 (2016).
27. P. C. Mondal, C. Fontanesi, D. H. Waldeck, R. Naaman, Spin-dependent transport through chiral molecules studied by spin-dependent electrochemistry. *Acc. Chem. Res.* **49**, 2560–2568 (2016).
28. P. C. Mondal, C. Fontanesi, D. H. Waldeck, R. Naaman, Field and chirality effects on electrochemical charge transfer rates: Spin dependent electrochemistry. *ACS Nano* **9**, 3377–3384 (2015).
29. W. Mtangi, V. Kiran, C. Fontanesi, R. Naaman, Role of the electron spin polarization in water splitting. *J. Phys. Chem. Lett.* **6**, 4916–4922 (2015).
30. D. G. Billing, A. Lemmerer, Synthesis and crystal structures of inorganic–organic hybrids incorporating an aromatic amine with a chiral functional group. *CrstEngComm* **8**, 686–695 (2006).
31. J. Ahn, E. Lee, J. Tan, W. Yang, B. Kim, J. Moon, A new class of chiral semiconductors: Chiral-organic-molecule-incorporating organic–inorganic hybrid perovskites. *Mater. Horiz.* **4**, 851–856 (2017).
32. C. Katan, N. Mercier, J. Even, Quantum and dielectric confinement effects in lower-dimensional hybrid perovskite semiconductors. *Chem. Rev.* **119**, 3140–3192 (2019).
33. A. Ben-Moshe, A. Teitelboim, D. Oron, G. Markovich, Probing the interaction of quantum dots with chiral capping molecules using circular dichroism spectroscopy. *Nano Lett.* **16**, 7467–7473 (2016).
34. Y. Zhou, M. Yang, K. Sun, Z. Tang, N. A. Kotov, Similar topological origin of chiral centers in organic and nanoscale inorganic structures: Effect of stabilizer chirality on optical isomerism and growth of cdte nanocrystals. *J. Am. Chem. Soc.* **132**, 6006–6013 (2010).
35. S. D. Elliott, M. P. Moloney, Y. K. Gun'ko, Chiral shells and achiral cores in CdS quantum dots. *Nano Lett.* **8**, 2452–2457 (2008).
36. V. Kiran, S. R. Cohen, R. Naaman, Structure dependent spin selectivity in electron transport through oligopeptides. *J. Chem. Phys.* **146**, 092302 (2016).
37. T. McGuire, R. Potter, Anisotropic magnetoresistance in ferromagnetic 3d alloys. *IEEE Trans. Magn.* **11**, 1018–1038 (1975).
38. Z. Xie, T. Z. Markus, S. R. Cohen, Z. Vager, R. Gutierrez, R. Naaman, Spin specific electron conduction through DNA oligomers. *Nano Lett.* **11**, 4652–4655 (2011).
39. Z. Xiong, D. Wu, Z. V. Vardeny, J. Shi, Giant magnetoresistance in organic spin-valves. *Nature* **427**, 821–824 (2004).
40. T. Zhang, M. Long, M. Qin, X. Lu, S. Chen, F. Xie, L. Gong, J. Chen, M. Chu, Q. Miao, Z. Chen, W. Xu, P. Liu, W. Xie, J.-b. Xu, Stable and efficient 3D-2D perovskite-perovskite planar heterojunction solar cell without organic hole transport layer. *Joule* **2**, 2706–2721 (2018).

Acknowledgments

Funding: This project was supported by the Center for Hybrid Organic Inorganic Semiconductors for Energy (CHOISE) an Energy Frontier Research Center funded by the Office of Basic Energy Sciences, Office of Science within the U.S. Department of Energy through contract number DE-AC36-08G028308. The views expressed in the article do not necessarily represent the views of the DOE or the U.S. Government. The U.S. Government retains and the publisher, by accepting the article for publication, acknowledges that the U.S. Government retains a nonexclusive, paid-up, irrevocable, worldwide license to publish or reproduce the published form of this work, or allow others to do so, for U.S. Government purposes. **Author contributions:** The project was planned by H.L., M.C.B., and Z.V.V. The samples were synthesized, prepared, and characterized by H.L. mCP-AFM measurements were conducted by C.X. MR device fabrication and measurements were conducted by J.W. and X.P. X.C. helped to model the linear absorption and CD spectra. R.B. measured the CD spectra. J.J.B. conducted the 2D XRD measurements. K.Z. provided important discussion. The manuscript was prepared by H.L., J.W., M.C.B., and Z.V.V and discussed with all other co-authors. **Competing interests:** The authors declare that they have no competing interest. **Data and materials availability:** All data needed to evaluate the conclusions in the paper are present in the paper and/or the Supplementary Materials. Additional data related to this paper may be requested from the authors.

Submitted 15 May 2019
Accepted 22 October 2019
Published 6 December 2019
10.1126/sciadv.aay0571

Citation: H. Lu, J. Wang, C. Xiao, X. Pan, X. Chen, R. Brunecky, J. J. Berry, K. Zhu, M. C. Beard, Z. V. Vardeny, Spin-dependent charge transport through 2D chiral hybrid lead-iodide perovskites. *Sci. Adv.* **5**, eaay0571 (2019).

ScienceAdvances

Spin-dependent charge transport through 2D chiral hybrid lead-iodide perovskites

Haipeng Lu, Jingying Wang, Chuanxiao Xiao, Xin Pan, Xihan Chen, Roman Brunecky, Joseph J. Berry, Kai Zhu, Matthew C. Beard, and Zeev Valy Vardeny

Sci. Adv. **5** (12), eaay0571. DOI: 10.1126/sciadv.aay0571

Science Advances (ISSN 2375-2548) is published by the American Association for the Advancement of Science. 1200 New York Avenue NW, Washington, DC 20005. The title *Science Advances* is a registered trademark of AAAS.